

Appendix A. Supplementary Information

Lead-free Monocrystalline Perovskite Resistive Switching Device for Temporal Information Processing

Jing-Yu Mao^a, Zhi Zheng^b, Zi-Yu Xiong^c, Pu Huang^c, Guang-Long Ding^a, Ruopeng Wang^{de}, Zhan-Peng Wang^a, Jia-Qin Yang^{de}, Ye Zhou^a, Tianyou Zhai^{*b} and Su-Ting Han^{*c}

^aInstitute for Advanced Study, Shenzhen University, Shenzhen 518060, P. R. China

^bState Key Laboratory of Material Processing and Die & Mould Technology, School of Materials Science and Engineering, Huazhong University of Science and Technology (HUST), Wuhan, 30074, P. R. China

^cCollege of Physics and Optoelectronics, Shenzhen University, Shenzhen, 518060, P. R. China

^dCollege of Electronics and Information Engineering, Shenzhen University, Shenzhen, 518060, P. R. China

^eInstitute of Micro Optoelectronics, Shenzhen University, Shenzhen, 518060, P. R. China

zhaity@hust.edu.cn

sutinghan@szu.edu.cn

DFT Calculation. The first-principle density function theory (DFT) calculations based on the projected augmented wave pseudopotential were conducted using the Vienna ab initio simulation package (VASP) code. The nudged elastic band method (NEB) was used to estimate the activation energy of bromide vacancy along the minimum migration path. DFT study was carried out under the condition of 0 K, and the $2\times 2\times 2$ supercell includes 112 atoms (14 atoms per unit cell) for the calculation of activation energy for bromide vacancy. The cutoff energy of 550 eV was selected for plane-wave basis set and the gamma point was sampled in the Brillouin zone integration. Atomic positions below $0.01 \text{ eV } \text{\AA}^{-1}$ were relaxed until the residual forces.

Experimental set-up for RC system. Five CSB diffusive RS devices were selected to compose the reservoir layer and the electrical characteristics were systematically measured. Each image is consisted of 25 (5×5) pixels. Each pixel-based image was splitted into 5 temporal pulse sequences by row to be delivered into the five selected devices that constitute the reservoir layer in order of row. Within one temporal pulse sequence, program pulse (6 V, 1 ms) and read pulse (0.5 V, 1 ms) are arranged with an interval time of 0.5 s according to the binary sequence. The pixel-based image is divided into 5 rows represented by 5 pulse sequences depending on the color of the pixel, which are fed into the 5 diffusive RS devices in the form of voltage pulses. The current states of the diffusive RS devices in the reservoir layer are considered as the reservoir states $x(t)$. During the input stage, each pulse sequence is fed into one

diffusive RS device and the current is recorded at a time according to the order of row.

The connection weights matrix θ between the input layer and the reservoir layer stays fixed of unit value. The readout function of the network is trained using logistic regression and the connection weight is updated after each training operation, which is all carried out in software. The output value is decided by both the reservoir state and the connection weight between the reservoir layer and the output layer. The probability is then calculated using sigmoid function.

$$h_{\theta}(x) = g(\theta^T \cdot x) = \frac{1}{1+e^{-\theta^T \cdot x}}$$

(1)

The cost function of logic regression is defined as log function instead of square root error as in the linear regression

$$J(\theta) = \frac{1}{m} \sum_{i=1}^m \left[-y^{(i)} \log(h_{\theta}(x^{(i)})) - (1 - y^{(i)}) \log(1 - h_{\theta}(x^{(i)})) \right] \quad (2)$$

where m is the number of training samples, $x^{(i)}$ is the input value and $y^{(i)}$ is the corresponding label value. The cost function is then minimized using the gradient descent

$$\frac{\partial J(\theta)}{\partial \theta_j} = \frac{1}{m} \sum_{i=1}^m (h_{\theta}(x^{(i)}) - y^{(i)}) x_j^{(i)} \quad (3)$$

In Matlab R2018a, optimal weights are obtained using function `fmincg()` which was provided by Carl Edward Rasmussen as a logistic regression routine with regularization and has been commonly used to classify handwritten digits.

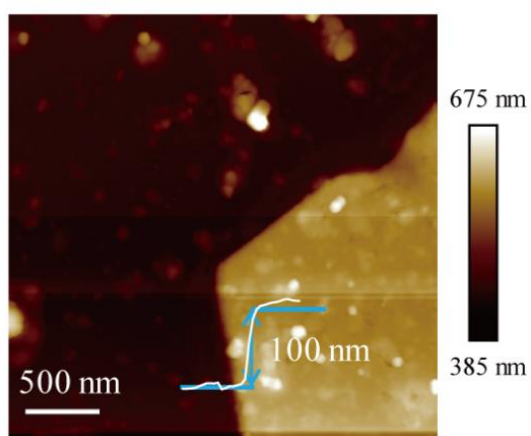


Fig. S1. AFM Image and height profile of a single crystal CSB nanoflakes.

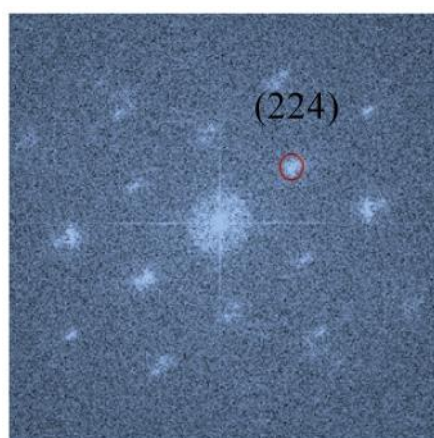


Fig. S2. Corresponding FFT image of single crystal CSB nanoflakes.

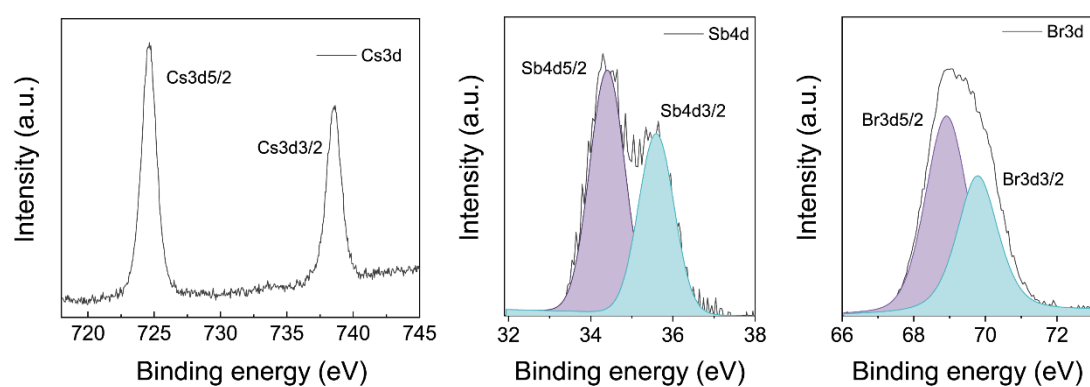


Fig. S3. XPS spectra for Cs_{3d}, Sb_{4d}, and Br_{3d} of CSB perovskite nanoflakes.

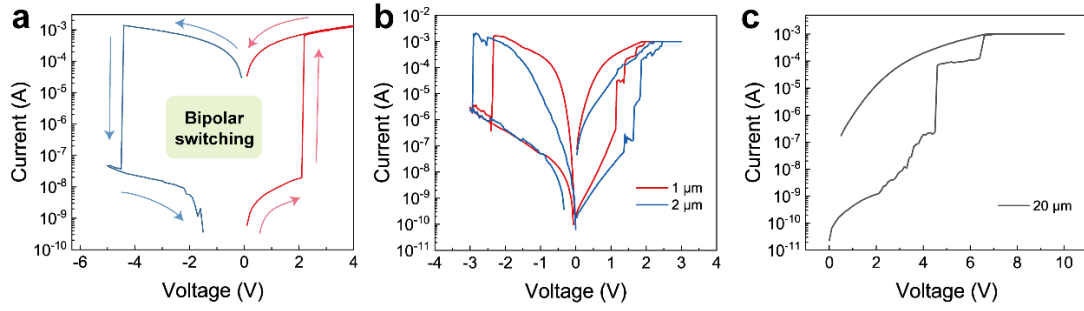


Fig. S4. Several representative I - V sweeps of CSB RS devices at short channel length of (a) 5 μm , (b) 1.2 μm and a long channel length of (c) 20 μm .

As the channel length is further shortened from 5 μm , higher operation currents were observed, which may lead to the deterioration of device electrical performance. RS devices with longer channel length result in unstable threshold switching behaviors.

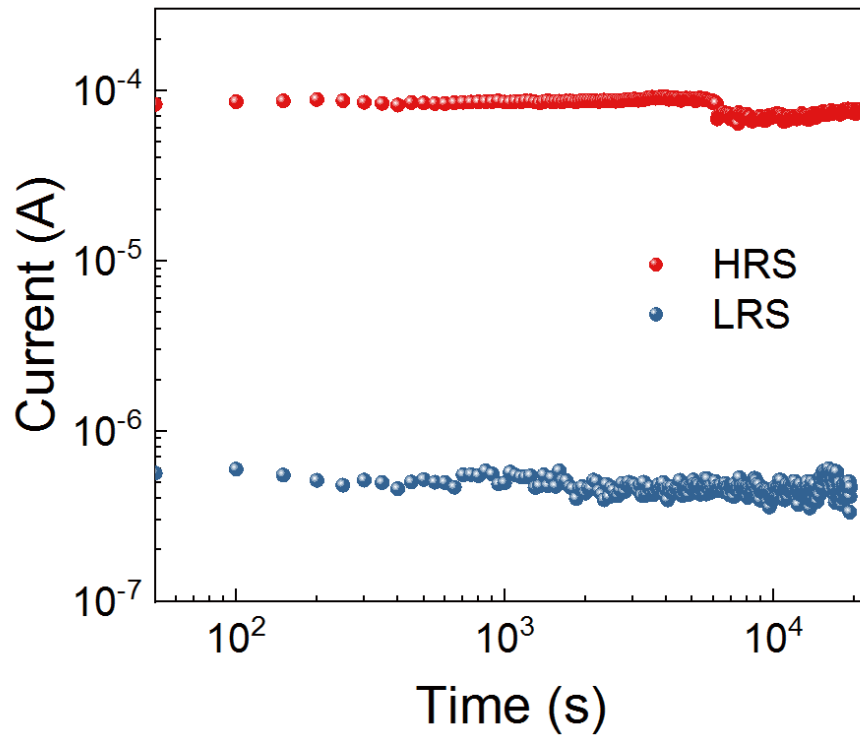


Fig. S5. Retention test for bipolar device at a read voltage of 0.5 V.

The long retention time indicates a nonvolatile behavior that LRS maintains its resistance state without additional power supply other than the read voltage pulse of

0.5 V. Both HRS and LRS exhibit stable current read under low bias (to avoid unexpected switching) without obvious fluctuation for over 2×10^4 s, demonstrating the capability of long data preservation with an average on/off ratio of 10^3 (CC is set to be 10^{-3} A to ensure the stability at LRS).

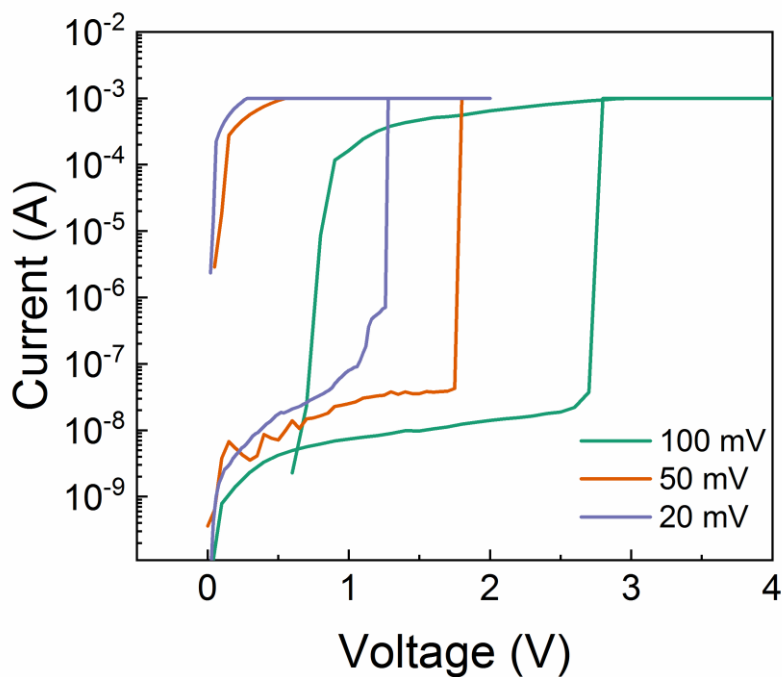


Fig. S6. *I-V* sweeps of different voltage steps.

Different steps of voltage sweeps were applied during measurements to show the effect on the SET voltage of the threshold switching event. As voltage step decreases, the threshold voltage is reduced due to the prolonged measurement for smaller step and possible more thorough Br ions migration. However, for step of 20 mV, an increase in the HRS current is observed.

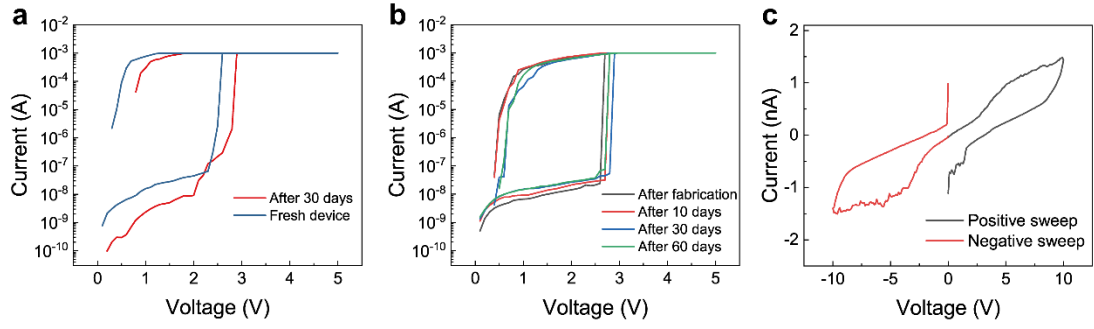


Fig. S7. I - V curves.

(a) Right after device fabrication and 30 days stored under air condition (b) CSB nanoflake based device with PVA coverage on top and (c) transferred PVA only without CSB nanoflake.

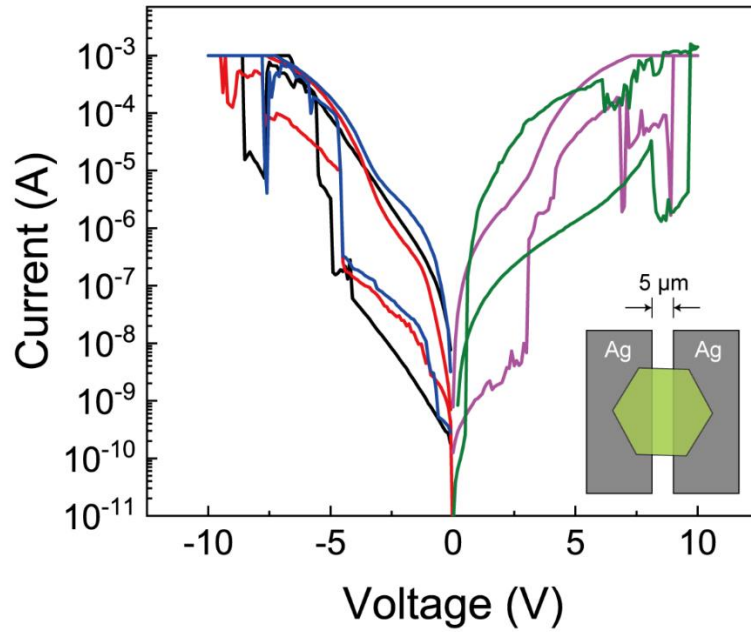


Fig. S8. Ag/Cs₃Sb₂Br₉/Ag device. Compared with Au/Cs₃Sb₂Br₉/Au device with the same channel length, larger value of threshold voltage was observed accompanied with unstable current fluctuation.

It is well known that active metal electrodes such as Ag and Cu normally are electrochemically active and often involve redox reaction at both electrodes allowing the formation and rupture of metal filaments. The introduction of active electrode material normally generates metal ions (in this case, Ag^+) penetration and migration from the anode to the cathode through the CSB nanoflake under electric field, followed by the redox reaction at material/electrode interface.

Studies on perovskite-based resistive memory often claimed that the dominating switching mechanism is Ag conductive filament. Normally, high electric field of over 10^7 V m^{-1} is required for the realization of ECM. Moreover, the introduction of Ag active electrode would make the underlying mechanism more obscure in terms of Ag filaments formation instead of the intrinsic property of perovskite materials itself. In this work, since both applied Au inert electrode are not electrochemically involved and migration of active metal ions can be excluded, thus the migration of intrinsic ions within the active material turns out to be the only vital issue to be taken into account.

Lead halide perovskites based resistive switching devices have already been reported with outstanding resistive switching behaviors including low switching voltage, multilevel storage and high on-off ratio. CSB RS devices reported here demonstrate superiorities of thermal stability, less sensitivity to moisture, superior to their toxic lead containing counterparts while retaining comparable switching performance. Unlike most of the studies of perovskite-based resistive switching devices that employ asymmetric combination of electrodes (such as Ag/ITO), here

planar perovskite memory device with symmetric device configuration of Au/Cs₃Sb₂Br₉/Au was fabricated and studied. Since most previous studies have investigated the resistive switching on nanosheets or nanoflakes mixed with polymers prepared by solution processing, the genuine cause for this behavior remains elusive. Therefore, single crystal perovskite-based devices possess the ability to help unambiguously elucidate the underlying operation mechanism within microscopic structures. For comparison, Ag/Cs₃Sb₂Br₉/Ag device was also fabricated to help elucidate the underlying mechanism of our perovskite memory, of which there exists to be a distinct electrical performance during voltage sweep, as shown in Figure S8. The introduction of active electrode material generates metal ions (in this case, Ag⁺) penetration and migration from the anode to the cathode through the perovskite under electric field. However, in view of AgBr complex formed in the electrode interface, the introduction of Ag as electrode may perplex the investigation into the resistive switching mechanism since metal-halide complex may be produced at the interfacial region near the electrode.

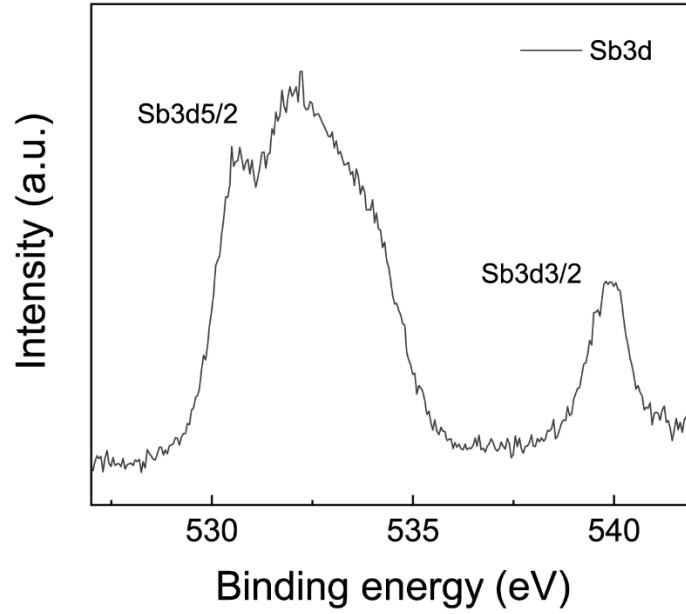


Fig. S9. XPS spectra for Sb_{3d}.

Sb⁰_{3d} peaks are not observed, indicating the sole effect of V_{Br}^{\bullet} 's migration responsible for resistive switching behavior.

Similar to the role of oxygen vacancies in the resistive switching in metal oxides, the resistive switching process in halide perovskite is greatly associated with the development of conductive filaments composed of halide vacancies of low-valence ions, which have been corroborated to be highly mobile with low activation energy while thermodynamically stable. Hence, vacancy-mediated diffusion and force driven by Joule heating become our major concerns to be responsible for different behaviors in resistive switching event. What's more important is that the electric field applied here ($2.2 \times 10^5 \text{ V m}^{-1}$) is extremely low comparing with that of devices based on other active materials, which could be explicit indication of the remarkably low activation energy for the migration of V_{Br}^{\bullet} 's under the guidance of electric field.

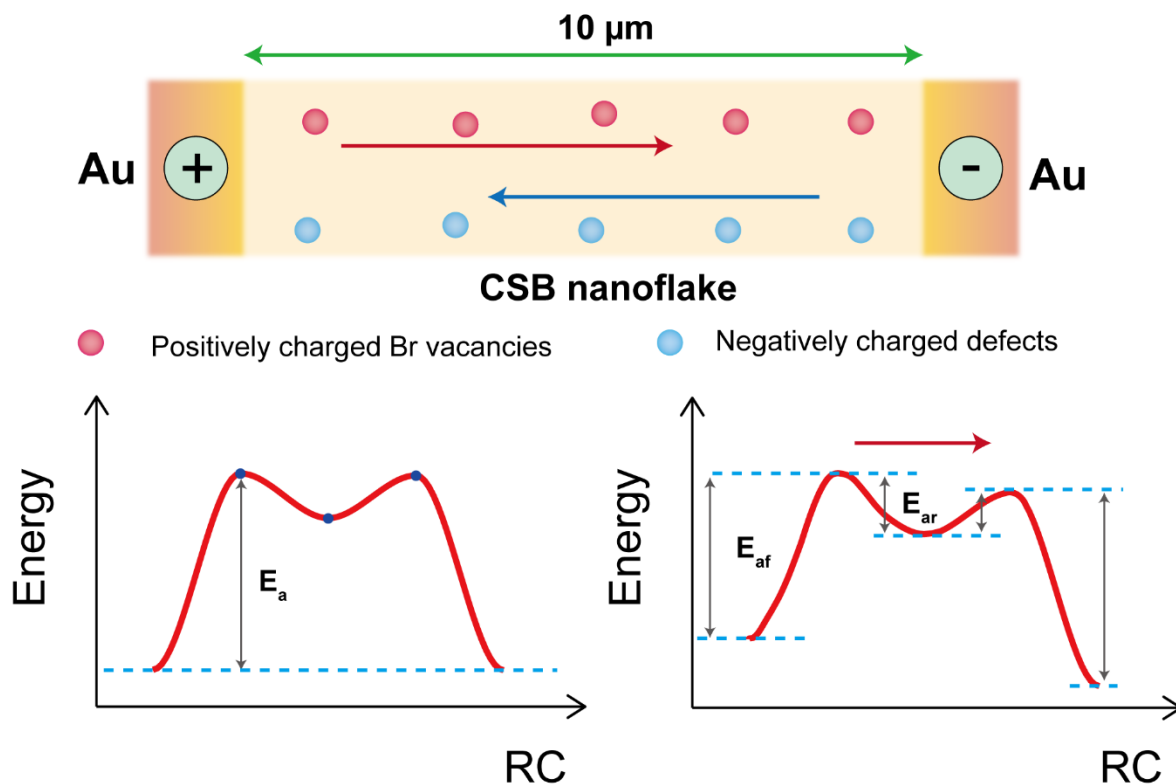


Fig. S10. Energy profiles for bromide vacancies migration through hopping between adjacent sites without and with electric field.

Without application of external electric field (initial condition), the activation energy profile for V_{Br} 's migration is displayed in the left side of Figure S10. Upon the application of electric field, V_{Br} 's were driven towards target electrode. The activation energy of V_{Br} 's hopping between different sites is different, giving rise to an asymmetric migration path, similar to that of MAPbBr_3 . Activation energy was lowered by about $\varepsilon/2$ for forward migration and suffered from an energy penalty of about $\varepsilon/2$. ε represents the variation in electrostatic energy across a unit cell. Therefore, the activation energies for forward and reverse direction become $E_{af} - \varepsilon/2$ and $E_{ar} + \varepsilon/2$, respectively, as shown in the energy diagram in the right side of Figure

S10. The migration rates constant for forward and backward hopping processes can be written as follows:

$$k_{forward} = \frac{k_B T}{\hbar} e^{-\frac{E_a - \varepsilon/2}{RT}} \quad (4)$$

$$k_{reverse} = \frac{k_B T}{\hbar} e^{-\frac{E_a + \varepsilon/2}{RT}} \quad (5)$$

The ratio of migration rate r (actual transport rate) can then be calculated by dividing the two equations:

$$r_{net} = \frac{k_{forward}}{k_{reverse}} = \frac{\frac{k_B T}{\hbar} e^{-\frac{E_a - \varepsilon/2}{RT}}}{\frac{k_B T}{\hbar} e^{-\frac{E_a + \varepsilon/2}{RT}}} = e^{\frac{\varepsilon}{RT}} \quad (6)$$

The actual efficiency for V_{Br} 's migration:

$$e = \frac{r_{net} + 1}{r_{net} - 1} \quad (7)$$

e stands for the proportion of actual step made forward to the total step made.

To simplify the calculation, we assume V_{Br} 's migrate along a one-dimensional path, thus the actual time required for the completion of V_{Br} 's reaching the opposite electrode will be longer. Obviously, deterministic factor is ε , which is associated with the potential difference and spacing between two electrodes. In this case, for a CSB diffusive RS devices with 10 μm channel length and voltage application of 5 V, the electric field is calculated to be 0.5 V μm^{-1} . So, in consideration of the length of unit

cell of 7.93 Å and the singly charged bromide vacancy ($1e$), ϵ of 0.3965 meV is acquired for each step towards the target electrode. r then holds a value of 1.16, indicating forward hopping process is 1.16 times faster than the reverse process (16 net steps every 216 steps). As an extreme situation, assuming that a bromide vacancy lies at one terminal, migration distance would be 10 μm which takes 12610 net forward steps to reach the opposite terminal. Since bromide vacancy migrates along half a unit cell, the total number of hops required will be 340470. The total time needed for a bromide vacancy to reach the counter electrode is obtained to be about 284 μs , which is expected to be reasonably fast considering such channel length. In view of the limits of experiment instruments and setup, resistive switching event triggered by electrical pulse with pulse width of 1 ms is most likely attributed to the migration of V_{Br}^{\bullet} 's.

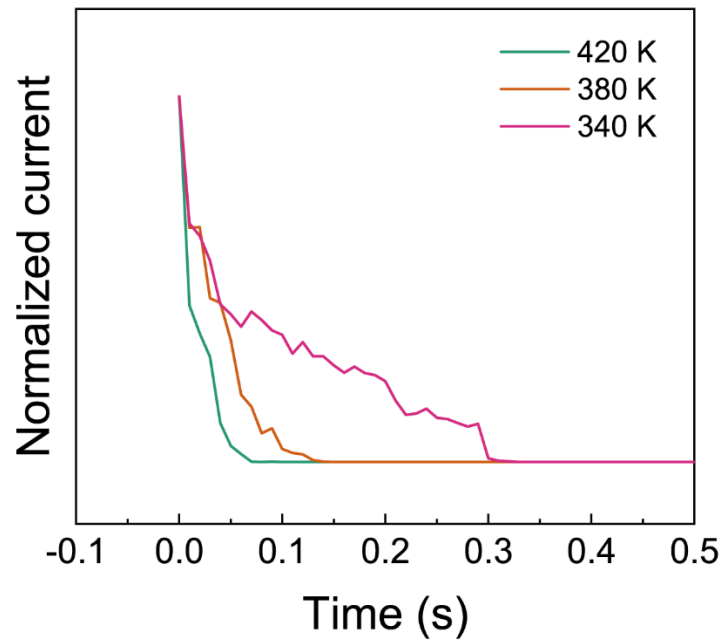


Fig. S11. Normalized current decay curves at different temperatures. Elevated temperature accelerates the relaxation process.

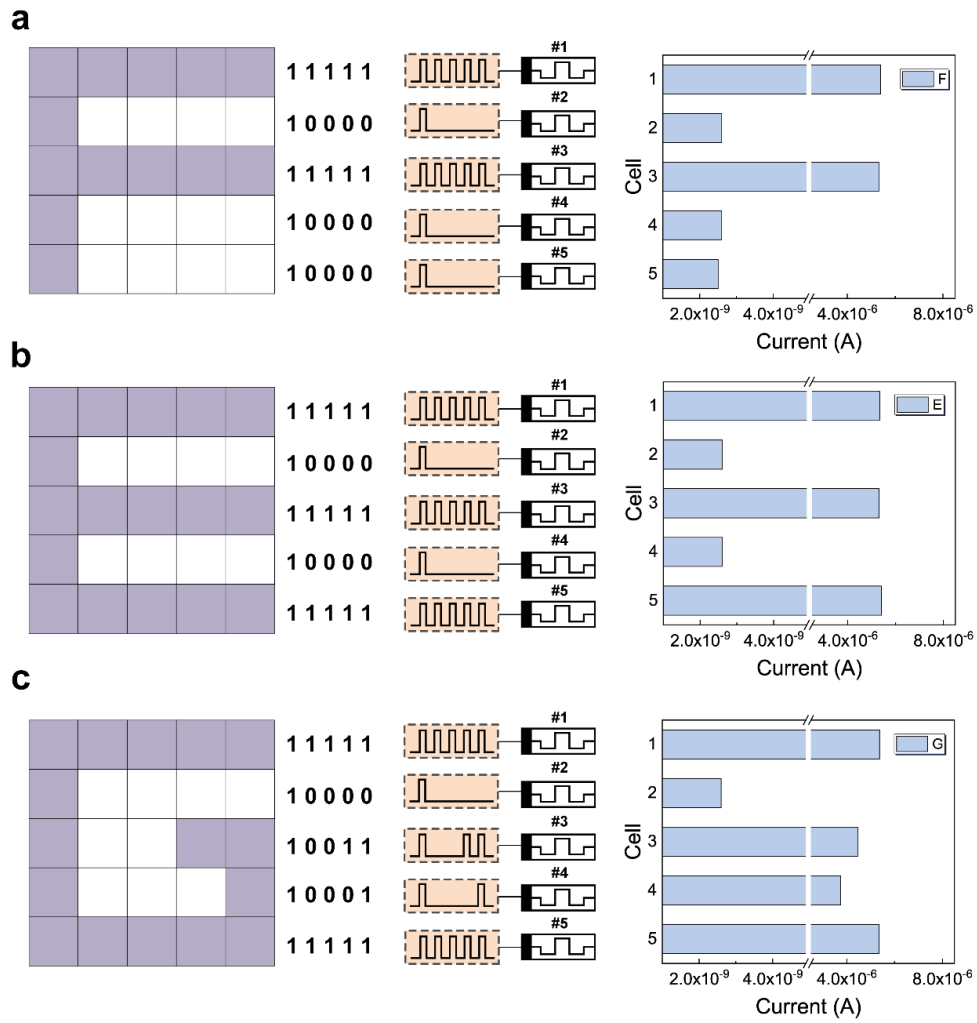


Fig. S12. (a) Letter “F”, (b) “E” and (c) “G” along with their input pulse sequences divided into each row and corresponding current responses after pulse sequence application for individual diffusive RS devices.

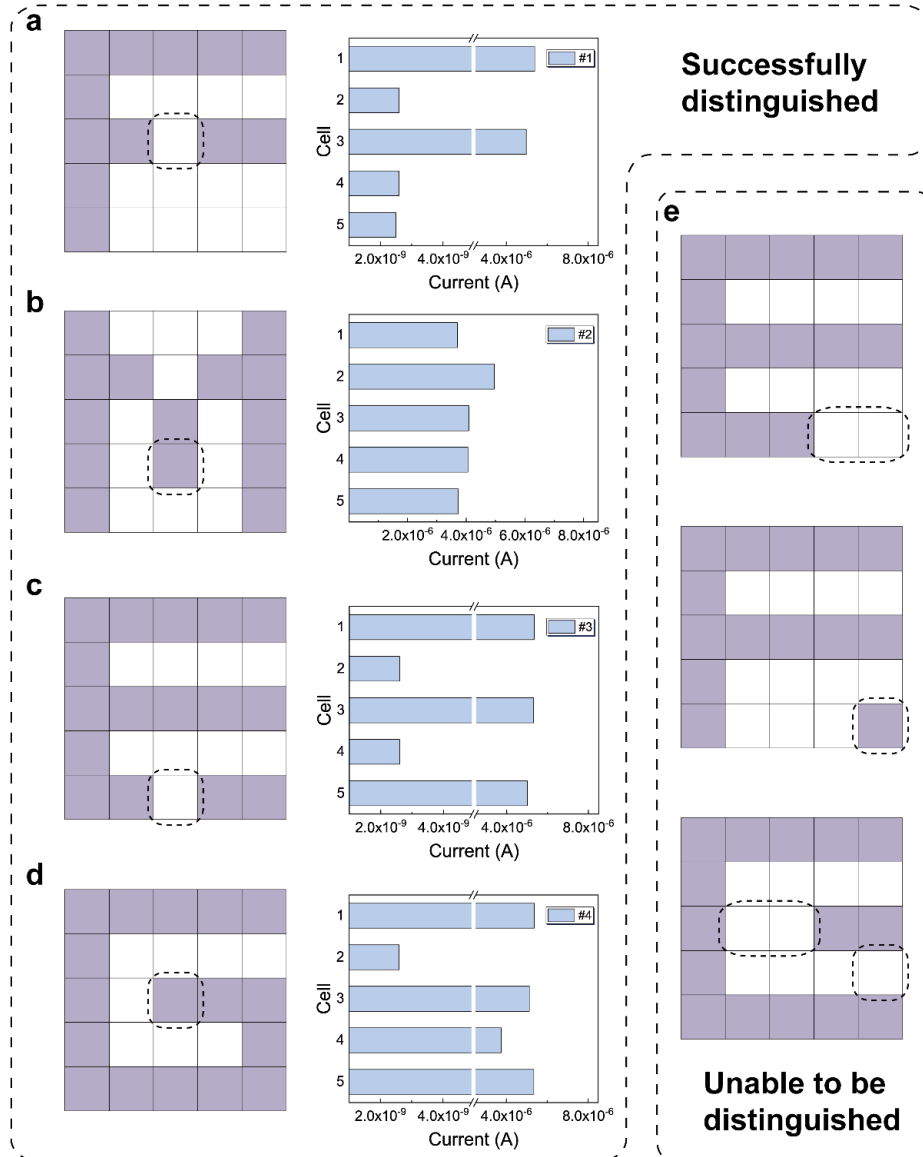


Fig. S13. Test samples and their corresponding current responses. (a) Test #1, (b) Test #2, (c) Test #3 and (d) Test #4. Three test samples in (e) are unable to be correctly distinguished due to their perplexity and similarity with more than one letter.